

pubs.acs.org/NanoLett Letter

# Thermomechanical Properties of Transition Metal Dichalcogenides Predicted by a Machine Learning Parameterized Force Field

Mohamed S. M. M. Ali, Hoang Nguyen, Jeffrey T. Paci, Yue Zhang, and Horacio D. Espinosa\*



Cite This: https://doi.org/10.1021/acs.nanolett.4c00285



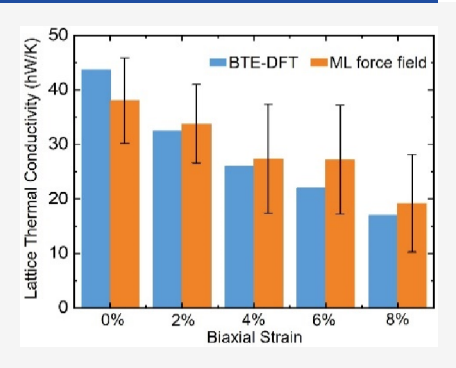
**ACCESS** I

III Metrics & More

Article Recommendations

SI Supporting Information

ABSTRACT: The mechanical and thermal properties of transition metal dichalcogenides (TMDs) are directly relevant to their applications in electronics, thermoelectric devices, and heat management systems. In this study, we use a machine learning (ML) approach to parametrize molecular dynamics (MD) force fields to predict the mechanical and thermal transport properties of a library of monolayered TMDs (MoS<sub>2</sub>, MoTe<sub>2</sub>, WSe<sub>2</sub>, WS<sub>2</sub>, and ReS<sub>2</sub>). The ML-trained force fields were then employed in equilibrium MD simulations to calculate the lattice thermal conductivities of the foregoing TMDs and to investigate how they are affected by small and large mechanical strains. Furthermore, using nonequilibrium MD, we studied thermal transport across grain boundaries. The presented approach provides a fast albeit accurate methodology to compute both mechanical and thermal properties of TMDs, especially for relatively large systems and spatially complex structures, where density functional theory computational cost is prohibitive.



KEYWORDS: transition metal dichalcogenides, thermal transport, strain engineering, machine learning force field

Because of their unique properties, transition metal dichalcogenides (TMDs) have been extensively investigated 1-9 to explore potential new applications, ranging from flexible electronics to wearable sensors and thermoelectric devices for energy production and storage. 10-14 Such applications almost always involve frequent mechanical deformations, such as stretching and bending, as well as thermal effects. Consequently, an accurate determination of mechanical and thermal properties of TMDs is indispensable to assess devices' integrity, reliability, and performance. Moreover, exploring the role of topological defects and structure—property relations in fracture and thermal transport mechanisms is crucial for the design and manufacturing of TMD heterostructures and devices.

A thorough understanding of TMDs' mechanical behavior and thermal transport mechanisms on a device level (hundreds of thousands of atoms), however, is still lacking. This, in part, can be attributed to the prohibitive computational costs of first-principles calculations and the often-encountered challenges of atomistic experimental investigations. These include sensitivity to samples' quality and size as well as the need for specialized testing setups that are capable of providing adequate resolution in force, displacement, and temperature measurements in real-time. Hence, molecular dynamics (MD) simulations guided by first-principles-trained force fields enable one to investigate the mechanical and thermal properties of TMDs for relatively large systems.

The predictive capability of MD relies on the force field used to describe interatomic interactions, as well as the set of properties used in their parametrization. Machine learning (ML)-based parametrization of interatomic potentials can approach density functional theory (DFT) accuracy while enabling bridging to continuum models. Force field parameters are typically determined to reproduce selected material properties computed from DFT and/or measured experimentally.<sup>8,18</sup> A common practice in parametrizing force fields is to use least-squares local minimization algorithms and a set of intuitively selected properties. There are several such examples in the literature for TMDs, e.g., for Mo–S systems,  $^{18-20}$  WS $_2$   $^{21,22}$  and WSe $_2$ . Our experience in using these previously parametrized force fields is that they fail to capture both mechanical stress in the large deformation regime and heat transport in the presence of defects, e.g., across grain boundaries (GBs). For instance, in a recent study, we reported that ReaxFF, parametrized for MoSe<sub>2</sub>, <sup>23</sup> could not capture the stress-strain behavior of the material in the large deformation regime. This motivated us to explore a global multiobjective optimization approach based on genetic algorithms (GAs) and data science, which have been demonstrated to be able to capture both near-equilibrium and far-from-equilibrium properties. 24,39,40 Indeed, we successfully compared atomistic structures and fracture energies, obtained from in situ high-

Received: January 19, 2024 Revised: June 20, 2024 Accepted: June 21, 2024



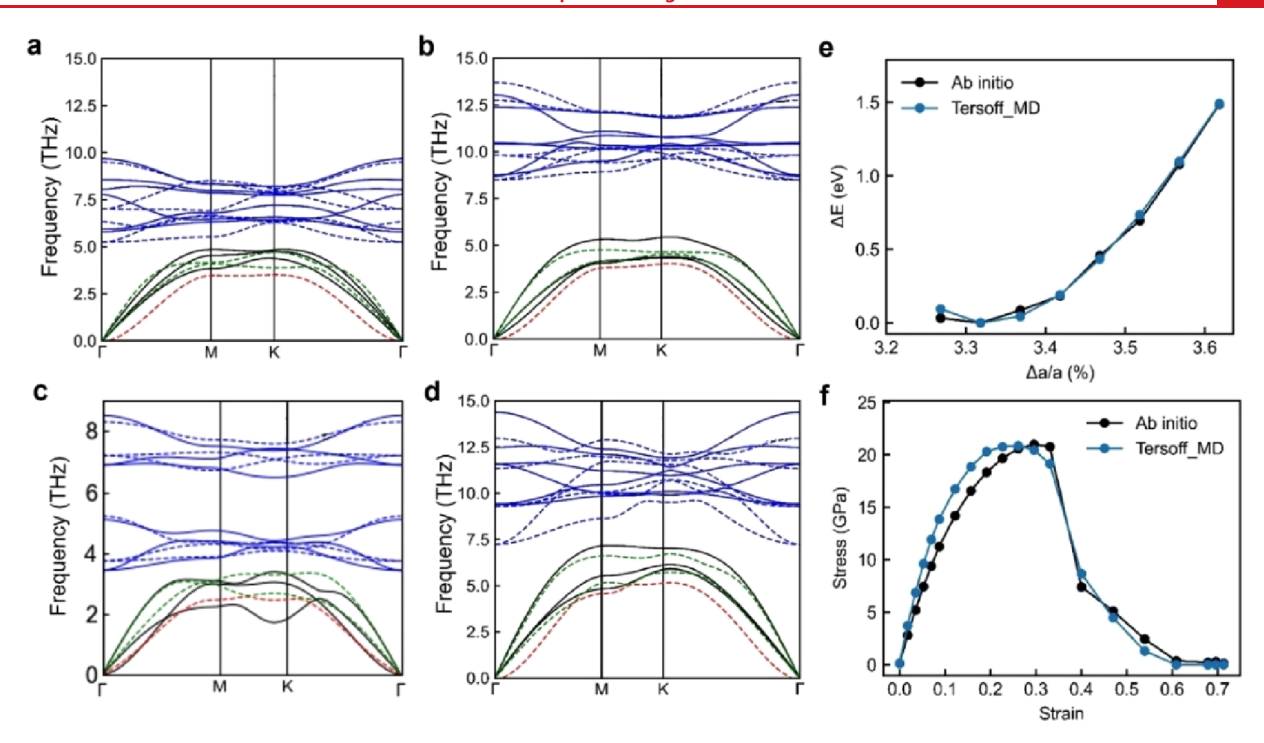


Figure 1. Predictions of thermal and mechanical properties for a library of TMDs. Comparisons of phonon dispersion curves are performed between MD and ab initio calculations for (a)  $WSe_2$ , (b)  $WSe_2$ , (c)  $MoTe_2$ , and (d)  $MoS_2$ . Optical modes are in blue (solid = ab initio; dashed = MD). Ab initio acoustic modes are in solid black, Tersoff ZA modes are in dashed red, and TA and LA modes are in dashed green. (e) Comparison of equation of state for monolayered  $WSe_2$ . (f) Comparison of perturbed uniaxial stress—strain curve along the armchair direction for monolayered  $WSe_2$ .

resolution transmission electron microscopy experiments, to MD simulations of the same structures using a multiobjective parametrized Tersoff potential.<sup>25</sup> The comparison revealed that bond breaking mechanisms, fracture energies, and atomic reconstructions at the crack edges were accurately described by the MD simulations.<sup>25</sup> Building on this success, in this work, we extend the methodology to parametrize the Tersoff force field for a library of TMDs (MoS<sub>2</sub>, MoTe<sub>2</sub>, WSe<sub>2</sub>, WSe<sub>2</sub>, ReS<sub>2</sub>) to reproduce both thermal conductivity and far-from-equilibrium mechanical properties, e.g., post-peak stress—strain relations leading to bond breakage (a key feature in assessing reliability). Furthermore, we illustrate the predictive capabilities of the Tersoff potential by investigating the effects of strain and GBs on the thermal transport of the TMDs mentioned above.

The Tersoff force field was first parametrized, for each TMD in the library (WS<sub>2</sub>, WSe<sub>2</sub>, MoS<sub>2</sub>, MoTe<sub>2</sub>, and ReS<sub>2</sub>), by means of a ML-based framework we previously reported (see Methods and Figure S1 for details).<sup>24</sup> The parametrized force field was then implemented in MD simulations to calculate the thermal and mechanical properties of the corresponding TMD's monolayers. In the present study, the primary goal is to explore the versatility and effectiveness of the parametrization framework across different TMDs. Therefore, we focus solely on the most stable phase of each TMD at room temperature (293 K). Other metastable phases (1T, 1T') can be investigated using the same approach but are left for future work. Furthermore, this investigation focuses on monolayer responses. Investigation of multilayered TMDs can employ the same force field parametrization framework by adding more training data and Lennard-Jones type interactions to include the interlayer van der Waals effect.

Phonon dispersion curves calculated using the parametrized Tersoff force field are shown in Figure 1a–d and Figure S2. The results indicate that, although optical phonons were not included in the parametrizations of the force fields, the algorithm captured the frequency gap between the acoustic and optical regimes, which is crucial to accurately predict phonon scattering processes in low conductivity monolayers, especially for WS<sub>2</sub> and MoS<sub>2</sub>. It is known that the larger the frequency gap, the less likely is the process of acoustic phonon annihilation, which explains why WS<sub>2</sub>, for instance, has a higher thermal conductivity than MoS<sub>2</sub>, despite the higher atomic mass of W compared to Mo. Furthermore, the absence of this acoustic-optical gap, in the case of ReS<sub>2</sub> (see Figure S2a), is the reason for its relatively small thermal conductivity.

The calculations of mechanical properties of WSe<sub>2</sub> are shown in Figure 1e,f and Figure S2b-f, which capture both equilibrium properties (e.g., equation of state) and far-fromequilibrium ones. Perturbed stresses refer to the soft modes, in which phonon instabilities are considered. Besides, the calculations of mechanical properties for the other four TMDs (WS<sub>2</sub>, MoS<sub>2</sub>, MoTe<sub>2</sub>, ReS<sub>2</sub>) are given in Figures S3-S7. These results indicate that the inclusion of nonequilibrium DFT training data in the parametrizations enables the accurate description of atomic behaviors in the large-deformation regime. The calculations of the other equilibrium properties (cohesive energy, elastic constants, and surface energies) of TMDs are summarized in Table S1. Moreover, Figure 1, Table S1, and Figures S2-S7 show that the calculations based on the parametrized Tersoff MD force fields agree with ab initio calculations, which validate the feasibility and precision of our ML-parametrized force fields in predicting the thermal and mechanical properties of TMDs.

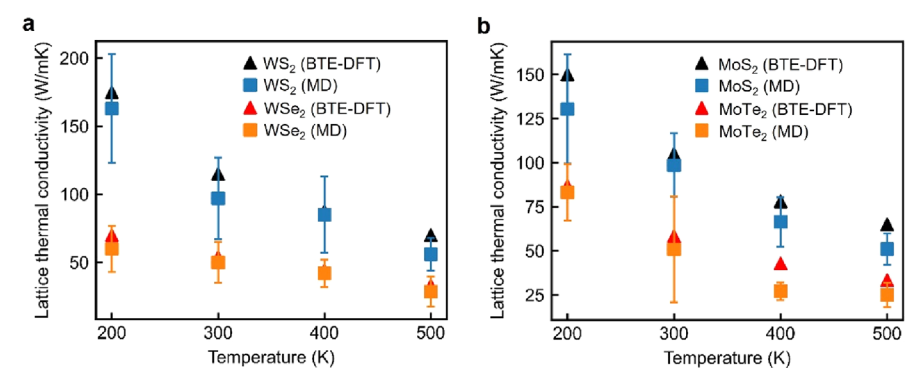
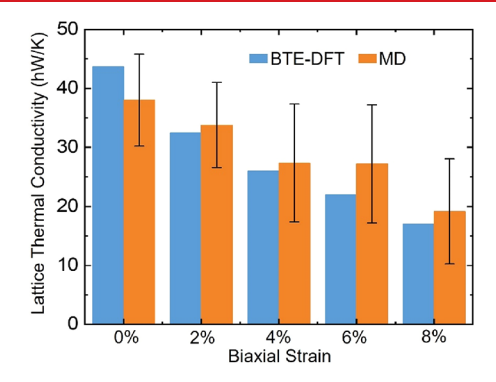


Figure 2. Lattice thermal conductivity for (a) WS<sub>2</sub> and WSe<sub>2</sub> and (b) MoTe<sub>2</sub> and MoS<sub>2</sub>, at different temperatures, predicted by the optimized Tersoff force fields and the ab initio Boltzmann transport equation (BTE-DFT).

Lattice thermal conductivities of the investigated TMDs library at different temperatures were also calculated using the parametrized Tersoff force fields; see Figure 2. To reduce the effect of random noise, the thermal conductivities were averaged over six MD runs with different initial velocities for each TMD. Convergence with respect to the effect of simulation cell size was also examined. Figure S8 illustrates the choice of the correlation time for thermal conductivity calculations, as an accurate choice of correlation time is crucial for equilibrium molecular dynamics (EMD) simulations to attain a converged state. For the WS $_2$  case, a correlation time of 1000 ps was chosen as it was long enough for the heat current autocorrelation function (HCACF) to decay to zero and the total thermal conductivity to converge.

These results indicate that the thermal conductivities of TMDs decrease with the increase of temperature. Besides, at a given temperature, the thermal conductivity of WS<sub>2</sub> is higher than that of WSe<sub>2</sub>, and the thermal conductivity of MoS<sub>2</sub> is higher than that of MoTe<sub>2</sub>. Moreover, it is shown that the mean thermal conductivities calculated from the parametrized MD force fields are in good agreement with the first-principles calculations using the Boltzmann transport equation (BTE-DFT). Figure S9 shows the calculations of thermal conductivity for ReS2, which is an interesting case because ReS<sub>2</sub> exhibits an absence of an acoustic-optical gap. The results were then compared with experimental measurements by Jang et al.<sup>27</sup> who reported thermal conductivity of ReS<sub>2</sub> samples with a total thickness of approximately 450 nm. Although such measured thermal conductivity corresponds to bulk ReS<sub>2</sub>, the conductivity loss due to the increased phonon scattering across layers should be negligible because van der Waals interactions between layers are weak compared to the covalent bonds within layers. Therefore, for comparison, we normalized the bulk measurement to a single-layer thickness. The calculation results closely match the experiment.

We further studied the effect of mechanical strains on the thermal conductivity of the studied TMDs using the parametrized force fields. As shown in Figure 3, the lattice thermal conductivity of the MoTe<sub>2</sub> monolayer, primarily contributed by acoustic phonons, decreases with the increase of an applied biaxial tensile strain. It also shows that the MD calculations are consistent with those of BTE-DFT. The decreasing thermal conductivity is due to the reduction in both the group velocity and phonon lifetime. Besides, it is known that shrinking the system size also reduces thermal conductivity by ruling out contributions from long meanfree-path phonons. The rate of decrease in thermal



**Figure 3.** Effect of biaxial tensile strains on lattice thermal conductivity for MoTe<sub>2</sub>. A comparison is made between MD calculations using the optimized Tersoff force fields and the ab initio Boltzmann transport equation (BTE-DFT).

conductivity, in the presence of tensile strain, is also found to be size-dependent. This dependence is attributed to the competition between phonon—phonon and phonon-boundary scattering. We note that, by capitalizing on the strain-dependent electronic structure of MoTe<sub>2</sub>, it becomes possible to tailor its properties for optimized thermoelectric performance. This discovery not only deepens our understanding of the material's behavior subjected to mechanical stress but also sets the stage for developing innovative, strain-engineered thermoelectric devices with enhanced energy conversion efficiency.

To illustrate the predictive capabilities of the parametrized force field for defective structures, we investigated the thermal transport of the studied TMDs across GBs. The nonequilibrium molecular dynamics (NEMD) method was used to calculate the thermal conductance across GBs. The thermal gradient can be established by adding and removing a predefined quantity of heat at specified distances, as shown in Figure 4a. Once the steady-state temperature profile was established, the temperature profile was combined with the known heat flux to calculate the Kapitza conductance, 29,30 which equals  $(Q/S)/\Delta T$ , where Q is the heat flux, S is the cross-sectional area, and  $\Delta T$  is the temperature difference across the GB interface. The GBs consisted of repeating five and seven-membered ring pairs (5-7 pairs) that were separated by hexagonal rings. Different misorientation angles of 9°, 14°, and 21° were modeled, where the defect concentration gradually increases (the number of separating hexagonal rings decreases). The temperature profile was determined by dividing the structure into sections that were

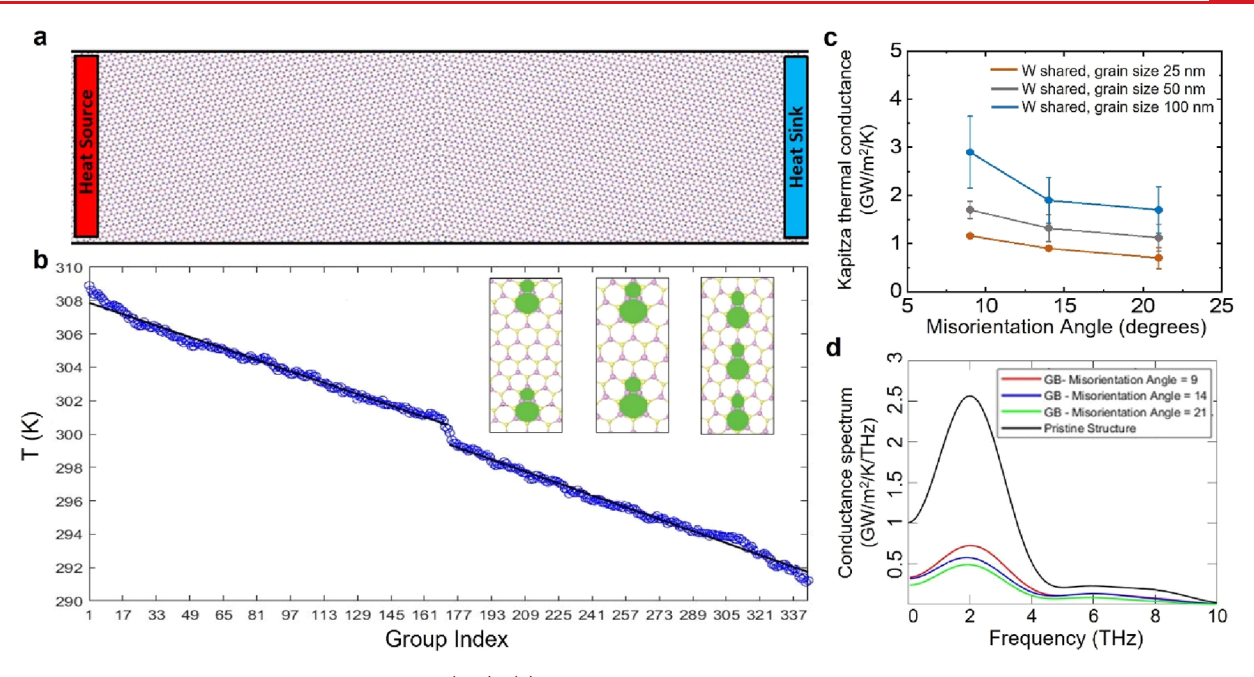


Figure 4. Thermal transport across grain boundaries (GB). (a) A schematic for the NEMD atomic model of WSe<sub>2</sub> with boundaries of a 5–7 GB symmetric structure. (b) Spatial distribution of temperature along the regions containing the two grains. The GB zone was used to determine the best linear fit (black lines) to evaluate the temperature gradient and hence to compute the thermal conductance across the GB. Inset: schematic of how defect concentration changes with the misorientation angle. (c) Effect of misorientation angle and grain size on the Kapitza thermal conductance across GBs. (d) Effect of the GB misorientation angle on the thermal conductance spectrum. Angles are reported in degrees.

Table 1. Interfacial (Kapitza) Conductance for Systems of 5-7 GB with Different Grain Sizes

	Misorientation Angle = $9^{\circ}$		Misorientation Angle = $14^{\circ}$		Misorientation Angle = $21^{\circ}$	
Kapitza Conductance (GW/m²K)	W - Shared	Se - Shared	W - Shared	Se - Shared	W - Shared	Se - Shared
Grain size, 25 nm	1.16	1.24	0.91	0.95	0.69	0.70
Grain size, 50 nm	1.71	1.57	1.32	1.32	1.12	0.93
Grain size, 100 nm	2.89	2.31	1.88	1.73	1.68	1.27

approximately 5 Å wide. The steady-state temperature profile along the heat transfer direction, shown in Figure 4b, revealed a temperature jump at the GB interface. Similar behavior has been reported for graphene<sup>31</sup> as well as MoS<sub>2</sub>.<sup>32</sup>

The effect of GBs' size and misorientation angle on Kapitza conductance was investigated and shown in Figure 4c and Figure S10. Two cases were assessed: Case (1), where W atoms occupied the shared pentagon-heptagon (5-7) GB edge, and case (2), where Se atoms constituted the shared edge. In both cases, the Kapitza conductance increases with GB size, as more phonons contribute to thermal transport. On the other hand, the conductance across the GB decreases as the misorientation angle increases, because the defect density increases with the misorientation angle. Interfacial thermal conductance, as calculated for different grain sizes and misorientation angles, is summarized in Table 1. The dependency of the Kapitza conductance on grain size reported here is consistent with the findings reported in the literature.<sup>31</sup> It was elucidated that, when grains are very large in size, the scattering of phonons within the grains primarily determines the thermal conductivity, but with decreasing grain size, the contribution to the thermal conductivity of the scattering from GBs, becomes more significant. In this study, we focused on a relatively small range of grain sizes, where scattering from GBs was dominant; thus, the grain size had a significant influence on the Kapitza conductance. It should be noted that, when the grain size becomes larger than those here investigated, the

Kapitza conductance will converge. In addition to the thermal conductance, the values of misorientation angle and grain size can also affect the mechanical properties such as elastic modulus and tensile strength of bicrystalline 2D materials. <sup>33,34</sup>

The virial velocity correlation function was calculated using eq 1. By taking its Fourier transform, we obtained the spectral conductance. As shown in Figure 4d, the peak of the conductance spectrum is reduced by increasing the misorientation angle, indicating strong phonon scattering at the GB interface.

$$K(t) = \sum_{i} \sum_{j \neq i} r_{ij}(0) \left\langle \left( \frac{\partial U_{j}}{\partial r_{ij}}(0) \cdot \frac{p_{i}(t)}{m_{i}} \right) \right\rangle; K(t)$$

$$= \sum_{i} \left\langle W_{i}(0) \cdot \nu_{i}(t) \right\rangle; \tilde{K}(\omega) = \int_{-\infty}^{\infty} e^{i\omega t} K(t) dt$$
(1)

In the conductance spectrum, it is observed that scattering of phonons is pronounced at a frequency of  $\sim$ 2 THz. For lower frequencies, scattering effects are attenuated. This can be explained as phonons with relatively large wavelengths act ballistically; i.e., if the phonon mean free path is larger than the grain size, phonons do not see the GBs. It can be inferred that optical phonons also contribute to the thermal conductance as is known for other nanostructures.  $^{35,36}$ 

To explore the mechanism responsible for the decrease in thermal conductivity of defective structures, as the defect

density increases, the phonon density of states (PDOS) was calculated using the Fourier transform of the velocity autocorrelation function from MD trajectories of atoms (Figure S11), namely,

$$F(\omega) = \frac{1}{\sqrt{2\pi}} \int_{-\infty}^{\infty} e^{-i\omega t} \langle v(t) \cdot v(0) \rangle / (\langle v(0) \cdot v(0) \rangle) dt$$
(2)

where  $F(\omega)$  represents the PDOS at angular frequency  $\omega$  and v(t) and v(0) represent the atomic velocity vectors at time t and 0, respectively.

A plot of the phonon density of states, Figure 5, reveals a mismatch between the GB cases and the pristine case. First,

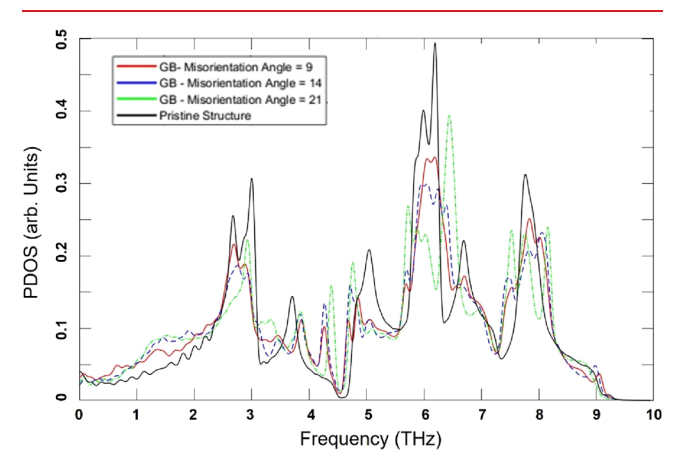


**Figure 5.** Phonon density of states for WSe<sub>2</sub>. Results are for the pristine structure as well as systems with grain boundaries of different misorientation angles. Angles are reported in degrees.

suppression and broadening of PDOS peaks, with an increase of the density of states at relatively low frequencies, indicate phonon mode localization. Besides, forbidden band gaps between acoustic and optical branches become narrower with GBs, indicating strong potential gradients around the GB cores, which leads to shorter phonon lifetimes and thus lower thermal conductance.

In conclusion, in this work, we report a ML-based framework to parametrize MD force fields, which enables accurate prediction of mechanical behavior at large strains simultaneously with phonon-dispersion relations for a library of TMDs. We then employed the parametrized force fields in MD simulations to investigate the thermal transport properties of TMDs. The investigation revealed that the implemented computational approach overcomes limitations in the BTE-DFT method, which accounts for only three or four phonon scattering processes. It is known that such limitations may result in an inaccurate prediction of phonon lifetimes and thus thermal conductivities. Furthermore, we employed the parametrized force fields in large-scale atomistic simulations, e.g., in the study of the effect of strains on the thermal conductivity of MoTe<sub>2</sub> and thermal transport across grain boundaries in WSe<sub>2</sub> strips. The versatility of the parametrized force fields became apparent when assessing the effect of strains and topological defects on thermal transport. In this context, the obtained force fields represent a powerful alternative for investigating the thermomechanical behavior of TMDs, especially for relatively large systems intractable by first-principles computations.

The computational approach reported in this work offers new simulation protocols for accurate and cost-effective predictions of the thermomechanical properties of TMDs. Such predictive capabilities are expected to impact the synthesis of these materials, and aid in the design and manufacturing of thermal functional devices such as thermal rectification devices with mechanically tunable features. Besides, the findings reported in this work also shed light on functional electronic devices with controllable thermal management through mechanical deformation. In closing, we note that the methodology is applicable to a variety of force fields including REBO, ReaxFF, and other ML force fields.

#### METHODS

The computational framework previously developed by Xu et al. was used to explore and predict the thermomechanical behavior of a library of TMDs. The training data set included both equilibrium and nonequilibrium properties, which were obtained from ab initio calculations. <sup>24,25</sup> For the equilibrium properties, we selected the cohesive energy of TMDs at equilibrium, the equation of state (near equilibrium), elastic constants ( $C_{11}$  and  $C_{12}$ ), and surface energies (armchair (AC) and zigzag (ZZ) surfaces), as given in Table S1 and Figure S3. For nonequilibrium properties, we selected the bond dissociation energy landscapes (along the AC and ZZ directions), vacancy formation energies, and uniaxial stressstrain curves (along the AC and ZZ directions), as given in Table S1 and Figures S4-S7. To generate nonequilibrium data sets, we selected a series of configurations with different strains and dissociation distances that cover the whole deformation process of TMDs. We utilized the procedure described by Akbar Ali and Violi<sup>37</sup> to predict and select the chemical pathways for dissociations of small clusters. Similar approaches have been adopted in the literature. 18,38,39 The DFT calculations were performed utilizing SIESTA software, which did not enforce the rotational sum rules.

In the training step, MD simulations with the same molecular structure used in DFT calculations but employing randomly generated Tersoff force field parameters were performed to compute the same target properties. The Tersoff functional form is given in Supplementary Note 1. Then, the Tersoff parameters were optimized simultaneously using the multiobjective framework mentioned above. A summary of this framework is presented in Figure S1, and the optimized Tersoff parameters are summarized in Tables S2–S6.

All MD simulations were performed using LAMMPS.<sup>41</sup> In the validation step, the ML parametrized Tersoff force fields were fed into EMD simulations to calculate the lattice thermal conductivity of a library of the studied TMDs with and without applied bi-axial strain. Furthermore, the NEMD simulations were used to study thermal transport across grain boundaries of selected TMDs. To be consistent with DFT calculations, we chose quasistatic simulations where the effect of strain rate is negligible.

MD-based methods for heat transport calculations exist in many flavors. 42-44 Upon proper choice of simulation parameters, both EMD and NEMD methods should yield consistent lattice thermal conductivities (LTCs) for the calculation of pristine structures. In the EMD method, the ensemble average of the heat current autocorrelation function was calculated according to the Green–Kubo relation. The Green–Kubo approach is chosen here because it is less sensitive to the domain size than the NEMD method. Besides, with the Green–Kubo method, the entire lattice thermal conductivity tensor can be calculated from one simulation,

unlike the NEMD method which necessitates several simulations in each direction to achieve the same. The Numerical integration is performed to compute the LTC,  $\kappa(t) = \frac{1}{k_{\rm B}T^2V} \int_0^t \langle J(t')J(0)\rangle \, \mathrm{d}t', \text{ where } k_{\rm B}T \text{ is the thermal energy and } V \text{ is the volume of the system. The EMD simulation is conducted as follows: First, we equilibrated the system for 0.1 ns in the NVT ensemble with a target temperature of 300 K. Second, we made a production run of 10 ns in the NVE ensemble, sampling the instant heat current every ten steps. Third, we calculated the heat current autocorrelation function using the saved heat current data and then calculated the LTC. We performed six independent runs and present the mean and error bars equal to one standard deviation.$ 

On the other hand, the NEMD method is based on Fourier's law of heat conduction. It can be used to calculate the thermal conductivity  $\kappa(L)$  of systems with finite length L, using the equation  $\kappa(L) = \frac{Q}{|\nabla T|}$ , where Q is an externally generated heat flux and  $\nabla T$  is the resulting temperature gradient in steady state. In the simulations, we fixed the two ends of the system in the transport direction and generated the heat flux by maintaining a temperature gradient with the local atomic groups close to the left end at 310 K (heat source) and close to the right end at 290 K (heat sink). Langevin thermostats were employed. The heat flux was calculated based on energy conservation between the system and the baths. The simulation was carried out as follows: First, we equilibrated the system for 0.1 ns in the NVT ensemble with a target temperature of 300 K. Second, we made a production run of 10 ns with local thermal baths, sampling the local temperatures and the accumulated energy exchanged between the system and the thermal baths. Third, we used the data within the last 6 ns of the production stage (where we checked that steady state had been achieved) to determine the temperature gradient  $\nabla T$ . The thermal conductivity was then calculated according to the above equation. Periodic boundary conditions were applied along the width. In order to cross-check results, another flavor of MD-based methods, namely, homogeneous nonequilibrium molecular dynamics (HNEMD),47 was implemented using GPUMD.

## ASSOCIATED CONTENT

## Supporting Information

The Supporting Information is available free of charge at https://pubs.acs.org/doi/10.1021/acs.nanolett.4c00285.

Figure showing machine learning parametrization framework, figures and tables showing comparison of ab initio data with predictions from parametrized Tersoff force fields, and notes and tables showing the functional form of parametrized Tersoff force fields (PDF)

## AUTHOR INFORMATION

### **Corresponding Author**

Horacio D. Espinosa — Department of Mechanical Engineering, Northwestern University, Evanston, Illinois 60208, United States; Theoretical and Applied Mechanics Program, Northwestern University, Evanston, Illinois 60208, United States; orcid.org/0000-0002-1907-3213; Email: espinosa@northwestern.edu

#### **Authors**

Mohamed S. M. M. Ali — Department of Mechanical Engineering, Northwestern University, Evanston, Illinois 60208, United States

Hoang Nguyen — Theoretical and Applied Mechanics
 Program, Northwestern University, Evanston, Illinois 60208,
 United States; Present Address: School of Engineering,
 Brown University, 184 Hope St., Providence, Rhode
 Island 02912, United States

Jeffrey T. Paci – Department of Chemistry, University of Victoria, Victoria, British Columbia V8W 3V6, Canada; orcid.org/0000-0003-4341-752X

Yue Zhang — Department of Mechanical Engineering, Northwestern University, Evanston, Illinois 60208, United States

Complete contact information is available at: https://pubs.acs.org/10.1021/acs.nanolett.4c00285

## **Author Contributions**

M.S.M.M.A. performed the MD simulations and thermal transport calculations. H.N. performed the DFT simulations. H.D.E. conceived and supervised the project. All authors contributed to the writing of the manuscript.

#### Note

The authors declare no competing financial interest.

#### ACKNOWLEDGMENTS

H.D.E. acknowledges the financial support from the Office of Naval Research (grant N000142212133), the Air Force Office of Scientific Research (AFOSR-FA9550-20-1-0258), and the National Science Foundation (grant CMMI-1953806).

## REFERENCES

- (1) Manzeli, S.; Ovchinnikov, D.; Pasquier, D.; Yazyev, O. V.; Kis, A. 2D transition metal dichalcogenides. *Nat. Rev. Mater.* **2017**, 2 (8), 1–15
- (2) Jardine, A.; Lee, E.; Ward, D.; Alexandrowicz, G.; Hedgeland, H.; Allison, W.; Ellis, J.; Pollak, E. Determination of the quantum contribution to the activated motion of hydrogen on a metal surface: H/Pt (111). *Physical review letters* **2010**, *105* (13), 136101.
- (3) Radisavljevic, B.; Radenovic, A.; Brivio, J.; Giacometti, V.; Kis, A. Single-layer MoS<sub>2</sub> transistors. *Nature Nanotechnol.* **2011**, *6* (3), 147–150.
- (4) Xia, D. D.; Gong, F.; Pei, X.; Wang, W.; Li, H.; Zeng, W.; Wu, M.; Papavassiliou, D. V. Molybdenum and tungsten disulfides-based nanocomposite films for energy storage and conversion: a review. *Chem. Eng. J.* 2018, 348, 908–928.
- (5) Cao, L.; Yang, S.; Gao, W.; Liu, Z.; Gong, Y.; Ma, L.; Shi, G.; Lei, S.; Zhang, Y.; Zhang, S. Direct laser patterned micro supercapacitors from paintable MoS<sub>2</sub> films. *small* **2013**, *9* (17), 2905–2910.
- (6) Nan, H.; Wang, Z.; Wang, W.; Liang, Z.; Lu, Y.; Chen, Q.; He, D.; Tan, P.; Miao, F.; Wang, X. Strong photoluminescence enhancement of MoS<sub>2</sub> through defect engineering and oxygen bonding. ACS Nano 2014, 8 (6), 5738–5745.
- (7) Patra, T. K.; Zhang, F.; Schulman, D. S.; Chan, H.; Cherukara, M. J.; Terrones, M.; Das, S.; Narayanan, B.; Sankaranarayanan, S. K. Defect dynamics in 2-D MoS<sub>2</sub> probed by using machine learning, atomistic simulations, and high-resolution microscopy. *ACS Nano* **2018**, *12* (8), 8006–8016.
- (8) Wang, S.; Qin, Z.; Jung, G. S.; Martin-Martinez, F. J.; Zhang, K.; Buehler, M. J.; Warner, J. H. Atomically sharp crack tips in monolayer MoS<sub>2</sub> and their enhanced toughness by vacancy defects. *ACS Nano* **2016**, *10* (11), 9831–9839.
- (9) Xu, X.; Chen, J.; Li, B. Phonon thermal conduction in novel 2D materials. J. Phys.: Condens. Matter 2016, 28 (48), 483001.

- (10) Jiang, D.; Liu, Z.; Xiao, Z.; Qian, Z.; Sun, Y.; Zeng, Z.; Wang, R. Flexible electronics based on 2D transition metal dichalcogenides. *Journal of Materials Chemistry A* **2021**, *10* (1), 89–121.
- (11) Aftab, S.; Hegazy, H. H.; Kabir, F. Emerging Trends in 2D Flexible Electronics. *Advanced Materials Technologies* **2023**, 8, 2201897.
- (12) Pallecchi, I.; Manca, N.; Patil, B.; Pellegrino, L.; Marré, D. Review on thermoelectric properties of transition metal dichalcogenides. *Nano Futures* **2020**, *4* (3), 032008.
- (13) Yun, Q.; Li, L.; Hu, Z.; Lu, Q.; Chen, B.; Zhang, H. Layered transition metal dichalcogenide based nanomaterials for electrochemical energy storage. *Adv. Mater.* **2020**, 32 (1), 1903826.
- (14) Yun, Q.; Lu, Q.; Zhang, X.; Tan, C.; Zhang, H. Three dimensional architectures constructed from transition metal dichalcogenide nanomaterials for electrochemical energy storage and conversion. *Angew. Chem., Int. Ed.* **2018**, *57* (3), 626–646.
- (15) Mortazavi, B.; Silani, M.; Podryabinkin, E. V.; Rabczuk, T.; Zhuang, X.; Shapeev, A. V. First principles multiscale modeling of mechanical properties in graphene/borophene heterostructures empowered by machine learning interatomic potentials. *Adv. Mater.* **2021**, 33 (35), 2102807.
- (16) Mortazavi, B.; Podryabinkin, E. V.; Roche, S.; Rabczuk, T.; Zhuang, X.; Shapeev, A. V. Machine-learning interatomic potentials enable first-principles multiscale modeling of lattice thermal conductivity in graphene/borophene heterostructures. *Materials Horizons* **2020**, *7* (9), 2359–2367.
- (17) Benedetti, I.; Nguyen, H.; Soler-Crespo, R. A.; Gao, W.; Mao, L.; Ghasemi, A.; Wen, J.; Nguyen, S.; Espinosa, H. D. Formulation and validation of a reduced order model of 2D materials exhibiting a two-phase microstructure as applied to graphene oxide. *Journal of the Mechanics and Physics of Solids* **2018**, *112*, 66–88.
- (18) Nayir, N.; Mao, Q.; Wang, T.; Kowalik, M.; Zhang, Y.; Wang, M.; Dwivedi, S.; Jeong, G.-U.; Shin, Y. K.; van Duin, A. C. Modeling and simulations for 2D materials: a ReaxFF perspective. 2D Materials 2023, 10 (3), 032002.
- (19) Liang, T.; Phillpot, S. R.; Sinnott, S. B. Parametrization of a reactive many-body potential for Mo-S systems. *Phys. Rev. B* **2009**, 79 (24), 245110.
- (20) Wen, M.; Shirodkar, S. N.; Plecháč, P.; Kaxiras, E.; Elliott, R. S.; Tadmor, E. B. A force-matching Stillinger-Weber potential for MoS<sub>2</sub>: Parameterization and Fisher information theory based sensitivity analysis. *J. Appl. Phys.* **2017**, *122* (24), 244301.
- (21) Nayir, N.; Shin, Y. K.; Wang, Y.; Sengul, M. Y.; Hickey, D. R.; Chubarov, M.; Choudhury, T. H.; Alem, N.; Redwing, J.; Crespi, V. H.; et al. A ReaxFF Force Field for 2D-WS<sub>2</sub> and Its Interaction with Sapphire. J. Phys. Chem. C 2021, 125 (32), 17950–17961.
- (22) Mobaraki, A.; Kandemir, A.; Yapicioglu, H.; Gülseren, O.; Sevik, C. Validation of inter-atomic potential for WS<sub>2</sub> and WSe<sub>2</sub> crystals through assessment of thermal transport properties. *Comput. Mater. Sci.* **2018**, *144*, 92–98.
- (23) Zhao, S.; Lu, M.; Xue, S.; Yan, L.; Miao, P.; Hang, Y.; Wang, X.; Liu, Z.; Wang, Y.; Tao, L. A Se vacancy induced localized Raman mode in two-dimensional MoSe<sub>2</sub> grown by CVD. *arXiv e-prints* **2019**, arXiv:1904.09789; DOI: 10.48550/arXiv.1904.09789 (accessed December 1, 2022).
- (24) Zhang, X.; Nguyen, H.; Paci, J. T.; Sankaranarayanan, S. K.; Mendoza-Cortes, J. L.; Espinosa, H. D. Multi-objective parametrization of interatomic potentials for large deformation pathways and fracture of two-dimensional materials. *npj Computational Materials* **2021**, *7* (1), 113.
- (25) Zhang, X.; Nguyen, H.; Zhang, X.; Ajayan, P. M.; Wen, J.; Espinosa, H. D. Atomistic measurement and modeling of intrinsic fracture toughness of two-dimensional materials. *Proc. Natl. Acad. Sci. U. S. A.* 2022, *119* (45), e2206756119.
- (26) Zhou, H.; Cai, Y.; Zhang, G.; Zhang, Y.-W. Unusual phonon behavior and ultra-low thermal conductance of monolayer InSe. *Nanoscale* **2018**, *10* (1), 480–487.

- (27) Jang, H.; Ryder, C. R.; Wood, J. D.; Hersam, M. C.; Cahill, D. G. 3D anisotropic thermal conductivity of exfoliated rhenium disulfide. *Adv. Mater.* **2017**, 29 (35), 1700650.
- (28) Zhang, Z.; Xie, Y.; Ouyang, Y.; Chen, Y. A systematic investigation of thermal conductivities of transition metal dichalcogenides. *Int. J. Heat Mass Transfer* **2017**, *108*, 417–422.
- (29) Zeng, T.; Chen, G. Phonon heat conduction in thin films: impacts of thermal boundary resistance and internal heat generation. *J. Heat Transfer* **2001**, *123* (2), 340–347.
- (30) Swartz, E. T.; Pohl, R. O. Thermal boundary resistance. Reviews of modern physics 1989, 61 (3), 605.
- (31) Bagri, A.; Kim, S.-P.; Ruoff, R. S.; Shenoy, V. B. Thermal transport across twin grain boundaries in polycrystalline graphene from nonequilibrium molecular dynamics simulations. *Nano Lett.* **2011**, *11* (9), 3917–3921.
- (32) Xu, K.; Liang, T.; Zhang, Z.; Cao, X.; Han, M.; Wei, N.; Wu, J. Grain boundary and misorientation angle-dependent thermal transport in single-layer  $MoS_2$ . *Nanoscale* **2022**, *14* (4), 1241–1249.
- (33) Grantab, R.; Shenoy, V. B.; Ruoff, R. S. Anomalous strength characteristics of tilt grain boundaries in graphene. *Science* **2010**, 330 (6006), 946–948.
- (34) Song, Z.; Artyukhov, V. I.; Yakobson, B. I.; Xu, Z. Pseudo Hall-Petch strength reduction in polycrystalline graphene. *Nano Lett.* **2013**, 13 (4), 1829–1833.
- (35) Tian, Z.; Esfarjani, K.; Shiomi, J.; Henry, A. S.; Chen, G. On the importance of optical phonons to thermal conductivity in nanostructures. *Appl. Phys. Lett.* **2011**, *99* (5), 053122.
- (36) Balandin, A. A. Nanophononics: phonon engineering in nanostructures and nanodevices. *J. Nanosci. Nanotechnol.* **2005**, 5 (7), 1015–1022.
- (37) Akbar Ali, M.; Violi, A. Reaction pathways for the thermal decomposition of methyl butanoate. *Journal of Organic Chemistry* **2013**, 78 (12), 5898–5908.
- (38) Mishra, A.; Hong, S.; Rajak, P.; Sheng, C.; Nomura, K.-i.; Kalia, R. K.; Nakano, A.; Vashishta, P. Multiobjective genetic training and uncertainty quantification of reactive force fields. *npj Computational Materials* **2018**, *4* (1), 42.
- (39) Chan, H.; Sasikumar, K.; Srinivasan, S.; Cherukara, M.; Narayanan, B.; Sankaranarayanan, S. K. Machine learning a bond order potential model to study thermal transport in WSe<sub>2</sub> nanostructures. *Nanoscale* **2019**, *11* (21), 10381–10392.
- (40) Chan, H.; Cherukara, M. J.; Narayanan, B.; Loeffler, T. D.; Benmore, C.; Gray, S. K.; Sankaranarayanan, S. K. Machine learning coarse grained models for water. *Nat. Commun.* **2019**, *10* (1), 379.
- (41) Thompson, A. P.; Aktulga, H. M.; Berger, R.; Bolintineanu, D. S.; Brown, W. M.; Crozier, P. S.; in 't Veld, P. J.; Kohlmeyer, A.; Moore, S. G.; Nguyen, T. D.; Shan, R.; Stevens, M. J.; Tranchida, J.; Trott, C.; Plimpton, S. J.; et al. LAMMPS a flexible simulation tool for particle-based materials modeling at the atomic, meso, and continuum scales. *Comp. Phys. Comm.* **2022**, 271, 108171.
- (42) Müller-Plathe, F. A simple nonequilibrium molecular dynamics method for calculating the thermal conductivity. *J. Chem. Phys.* **1997**, 106 (14), 6082–6085.
- (43) Müller-Plathe, F.; Reith, D. Cause and effect reversed in non-equilibrium molecular dynamics: an easy route to transport coefficients. *Comput. Theor. Polym. Sci.* **1999**, 9 (3–4), 203–209.
- (44) Lee, Y. H.; Biswas, R.; Soukoulis, C. M.; Wang, C.; Chan, C. T.; Ho, K. Molecular-dynamics simulation of thermal conductivity in amorphous silicon. *Phys. Rev. B* **1991**, 43 (8), 6573.
- (45) Dongre, B.; Wang, T.; Madsen, G. K. Comparison of the Green-Kubo and homogeneous non-equilibrium molecular dynamics methods for calculating thermal conductivity. *Modell. Simul. Mater. Sci. Eng.* **2017**, *25* (5), 054001.
- (46) McQuarrie, D. Statistical Mechanics; Harper & Row, 1976.
- (47) Lampin, E.; Palla, P. L.; Francioso, P.-A.; Cleri, F. Thermal conductivity from approach-to-equilibrium molecular dynamics. *J. Appl. Phys.* **2013**, *114* (3), 033525.